An efficient integration technique for the voxel-based Finite Cell Method

Z. Yang[1,*], M. Ruess[1], S. Kollmannsberger[1], A. Düster[2], E. Rank[1]

[1] Chair for Computation in Engineering, Technische Universität München, Arcisstraße 21, 80333 Munich, Germany [2] Numerische Strukturanalyse mit Anwendungen in der Schiffstechnik (M-10), Technische Universit¨at Hamburg-Harburg, Schwarzenbergstr. 95c, 21073 Hamburg, Germany

Abstract

The Finite Cell Method (FCM) is a fictitious domain approach based on hierarchical Ansatz spaces of higher order. The method avoids time-consuming and often error-prone mesh-generation and favorably exploits Cartesian grids to embed structures of complex geometry in a simple shaped computational domain thus shifting parts of the computational effort from mesh generation to the computation within the embedding finite cells of regular shape. This paper presents an effective integration approach for voxel-based models of linear elasticity that drastically reduces the computational effort on cell level. The applied strategy allows the pre-computation of an essential part of the cell matrices and vectors of higher order, representing stiffness and load, respectively. Several benchmark problems show the potential of the proposed method in particular for heterogeneous material properties as common in biomedical applications based on computer tomography scans. The applied strategy ensures a fast computation for time-critical simulations and even allows user-interactive simulations for models of moderate size at a high level of accuracy.

Keywords: fictitious domain method; Finite Cell Method; voxel models; high-order FEM; solid mechanics

1 Introduction

Voxel models generated by recursive bisection [13, 36] or derived from x-ray images and quantitative computer tomography scans (qCT-scan), respectively, are often used to overcome a time-consuming and error-prone mesh-generation for the numerical simulation of structures of high geometric complexity. Such simulations include e.g. seismic analyses and ground water flow in soil mechanics [16, 6], shape and topology optimization of complicated structures [9, 21, 1, 33], stability analyses of foam structures [25] and numerous examples from biomedical fields as bone [24, 39, 40, 23, 17] or dental mechanics [18, 14]. For Finite Element schemes the voxel approach avoids fine granular meshes but still is often limited in terms of accuracy due to a constant element-wise material assignment. In particular in terms of computational efficiency it often requires means of parallelization to generate solutions with a reasonable time effort [34, 19, 8].

*Corresponding author:
Chair for Computation in Engineering, Technische Universität München, Arcisstraße 21, 80333 Munich, Germany, email: yang@bv.tu-muenchen.de

The following contribution introduces an extension of the Finite Cell Method [20, 10], a high order fictitious domain method that favorably applies the simple nature of Cartesian grids and turns out to be highly suited for time-critical voxel-based simulations of complex structures in various fields of numerical simulation. The Finite Cell Method recently has been successfully applied for geometrically nonlinear analyses of foam-like structures with various refinement strategies [26, 25], advection-diffusion problems [6] and applications in the field of bone mechanics [24] as well as to the numerical homogenization of heterogeneous and foamed materials [28, 11]. With the extension of a pre-computation scheme the method even is capable to produce sufficient update rates for user-interactive simulations in patient-specific femur analyses [38]. The developments described in the following focus on a time-efficient extension of the FCM for linear elasticity problems that partly can be applied also for the linearized equations of non-linear problems. However the major effort of such problems remains computationally expensive and cannot directly profit from the presented concepts. Beside the algorithmic reduction of the time complexity the performance of the implementation profits from a multi-core parallelization with expected parallel efficiency on eight cores. Owing to the exploited Ansatz space of higher order [32, 31], the method provides properties comparable to the p-FEM with regard to convergence behavior and error control. A flexible sub-cell integration scheme proposed in [10] allows to accurately capture multi-material interfaces and heterogeneous material distributions as common in biomedical problems, a scheme that serves as basis for the proposed extension in this contribution.
This paper is organized as follows: Section 2 provides a brief overview about the basic idea of the Finite Cell Method. Section 3 introduces the fast integration concept for three-dimensional problems with a special focus on qCT-derived voxel data. Section 4 provides three numerical examples to illustrate the performance of the proposed method. The paper is summarized with the conclusions in Section 5.

2 The Finite Cell Method

The Finite Cell Method [20, 10] is a fictitious domain method based on high-order polynomial Ansatz spaces that embeds the physical domain Ω of arbitrary complex geometry in an extended, fictitious domain Ω_{FD} of significantly simpler shape (Fig. 1). The method favorably exploits the properties of Cartesian grids and thus avoids numerically expensive mesh generation.

The grid structure is applied to decompose the embedding domain Ω_{FD} into a set of finite cells Ω_C covering the physical domain Ω. Cells that are completely outside Ω are discarded to reduce the effort of computation and to support numerical stability of the formulation. In general the cell boundary $\partial\Omega_C$ is assumed traction free. Homogeneous and inhomogeneous Dirichlet and Neumann boundary conditions of the physical domain are directly applied to the boundary $\Gamma_D \cup \Gamma_N = \Gamma$. Surface traction on the non-homogeneous Neumann boundary Γ_N is applied by integration over a parametrized surface patch on Γ that can be obtained with negligible effort e.g. from a locally confined triangulation. In [10] the application of Neumann boundary conditions on the embedded structure is discussed in detail.

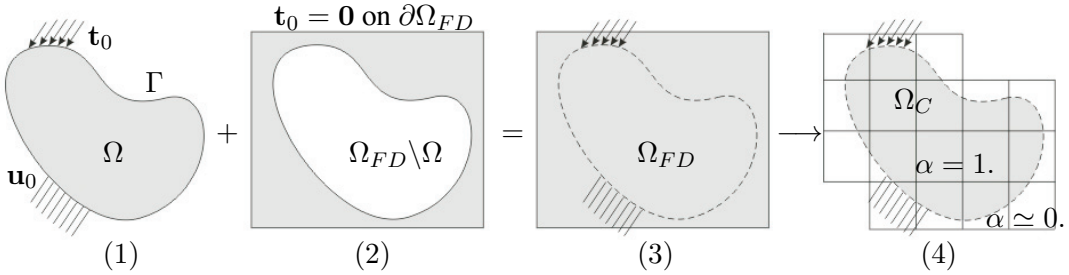

Figure 1: (1) Physical domain Ω with prescribed traction $\mathbf{t}_0$ along the Neumann boundary Γ_N and prescribed displacements $\mathbf{u}_0$ along the Dirichlet boundary Γ_D, (2) extended cell domain $\Omega_{FD}\backslash\Omega$ with zero traction $\mathbf{t}_0$ on the cell domain surface $\partial\Omega_{FD}$, (3) embedded domain with implicit domain support for Ω_{FD} from prescribed displacement constraints on Γ_D and (4) applied cell grid structure on Ω_C with indicator function α.

Various studies show that a weak enforcement of Dirichlet boundary conditions provide a reliable strategy to prescribe primals at arbitrary positions along Γ_D. So far the penalty method [35] and a Nitsche type weak enforcement [24] of the essential boundary conditions have been tested successfully.

With penalization of the stress tensor $\boldsymbol{\sigma}(\alpha) = \alpha\,\boldsymbol{\sigma}$ in the fictitious domain the formulation ensures consistency with the original problem. The function $\alpha(\mathbf{x})$ indicates the true structure Ω within the fictitious domain of the cell structure

$$\alpha(\mathbf{x}) \;=\; \begin{cases} \alpha \;=\; 1 & \forall\, \mathbf{x} \in \Omega \\ \alpha \;=\; \epsilon & \forall\, \mathbf{x} \in \Omega_C \setminus \Omega \end{cases} \tag{1}$$

with ϵ chosen small enough to account for the physical domain only. Typical values for ϵ vary in the range between 10^{-4} and 10^{-14} and can be found e.g. in dependence of the stiffness of the structure to ensure both, accuracy and numerical stability [24].
With (1) the weak formulation of the linear elasticity problem for the extended problem is specified according to the principle of virtual work

$$\delta W_\sigma(\mathbf{u}, \delta\mathbf{u}) \;=\; \int_{\Omega_C} \delta\boldsymbol{\varepsilon} : \boldsymbol{\sigma}(\alpha)\, d\Omega - \int_{\Omega_C} \delta\mathbf{u} \cdot \mathbf{p}(\alpha)\, d\Omega \;-\; \int_{\Gamma_N} \delta\mathbf{u} \cdot \mathbf{t}_0\, d\Gamma \;=\; 0 \tag{2}$$

including the displacement vector $\mathbf{u}$, linear strains $\boldsymbol{\varepsilon}$, the virtual quantities $\delta\mathbf{u}$ and $\delta\boldsymbol{\varepsilon}$ and the volume load vector $\mathbf{p}$. The volume loads in the fictitious part of Ω_C are penalized in analogy to the stresses with α.
The Finite Cells are implemented as hexahedral elements according to the principles of tensor product elements of the Finite Element Method. The unknown displacement field $\mathbf{u}(\mathbf{x})$ is approximated with hierarchical piecewise defined polynomials of higher order $N_i(\xi, \eta, \zeta)$ specified

in the standard hexahedral $(-1 \leq \xi, \eta, \zeta \leq 1)$ (see [30])

$$\mathbf{u} = \sum_a \mathbf{N}_a(\xi, \eta, \zeta)\, \mathbf{U}_a \tag{3}$$

$$\delta\mathbf{u} = \sum_a \mathbf{N}_a(\xi, \eta, \zeta)\, \delta\mathbf{U}_a \tag{4}$$

with $\mathbf{U}_a$ and $\delta\mathbf{U}_a$ denoting the unknown degrees of freedom. The approximation of the linear strain tensor $\boldsymbol{\epsilon}$ and corresponding virtual quantity applies the standard strain operator $\mathbf{B}(\xi, \eta, \zeta)$ that is obtained from differentiation of (3) with respect to the global coordinates (x, y, z), applying the chain rule.
Following the Bubnov-Galerkin approach equations (3) and (4) are substituted into the weak form (2) providing a discrete finite cell formulation

$$\mathbf{K}\,\mathbf{U}_a = \mathbf{P} \tag{5}$$

with the $(N \times N)$-matrix $\mathbf{K}$ representing the system stiffness and corresponding system load vector $\mathbf{P}$.

3 Cell integration scheme for voxel data

Rapid and simple grid generation is one of the major advantages of the Finite Cell Method as compared with tedious and often error-prone mesh generation for complex domain geometries or multi-material interfaces. With the indicator function $\alpha(\mathbf{x})$, specified in the previous section, that decides if points are inside or outside the physical domain, an essential part of the modeling effort is shifted to the governing integrals on cell level. The integrals (6) and (7) are computed numerically with Gauss quadrature. In the general case of non-voxelized solid structures an adaptive integration scheme is necessary to accurately capture the true boundary of the physical domain and to confine the integration error and the numerical effort [26]. In [10] a sub-cell strategy is introduced that allows to arbitrarily densify the quadrature points within Ω_C thus supporting adaptive integration on various granularity levels. In combination with a locally restricted octree generation that turns out to be an efficient and fast voxelization approach, the true domain is accurately identified (see e.g. [26, 25, 10]).
The shape of voxelized domains is directly given either by the assembly of voxels or by the value of each voxel in the case of qCT-derived voxel data. For both cases a regular sub-cell scheme is applied, decomposing each finite cell into $(m_x \times m_y \times m_z)$ sub-cells for integration.
The number of quadrature points required to exactly integrate polynomials depends on the polynomial degree. Despite the polynomial character of the integral (6) that has a constant and diagonal Jacobian $\mathbf{J}$, $(p+1)^3$ quadrature points are in general applied for integration of cells with shape functions of degree p. Accepting an approximation error of negligible size, the sub-cell approach allows a reduction of the number of quadrature points for each sub-cell and even more it ensures a regular distribution to best possibly capture a discrete material distribution of heterogeneous material properties.

3.1 Pre-computation on cell level

With the quantities $\mathbf{u}$, $\delta\mathbf{u}$ and $\boldsymbol{\varepsilon}$ defined in the previous section, the stiffness matrix of cell c can be obtained resulting in

$$\mathbf{K}_c = \int_\xi \int_\eta \int_\zeta \mathbf{B}^T \alpha\, \mathbf{C}\, \mathbf{B}\, det\mathbf{J}\, d\zeta d\eta d\xi \tag{6}$$

with a constant and diagonal Jacobi matrix $\mathbf{J}$ of the cell geometry mapping and the elasticity matrix $\mathbf{C}$. Similarly the cell volume load vector is given as

$$\mathbf{P}_c = \int_\xi \int_\eta \int_\zeta \mathbf{N}^T \alpha\, \mathbf{p}\; det\mathbf{J}\, d\xi d\eta d\zeta \tag{7}$$

For a pre-computation of the integrals (6) and (7) the following strategy is applied: The material properties of the $(n_x \times n_y \times n_z)$ voxels per finite cell are assumed constant for each voxel. This is especially true for qCT-derived voxel data and is favorably exploited to model a discrete and heterogeneous material distribution. With this property the integrals (6) and (7) representing cell stiffness and cell load, respectively, are replaced by the sum over $(n_x \times n_y \times n_z)$-integrals, each defined over the domain of a single voxel:

$$\hat{\mathbf{K}}_c = \sum_{i=1}^{n_z} \sum_{j=1}^{n_y} \sum_{k=1}^{n_x} \mathbf{K}_{ijk} \tag{8}$$

$$\hat{\mathbf{P}}_c = \sum_{i=1}^{n_z} \sum_{j=1}^{n_y} \sum_{k=1}^{n_x} \mathbf{P}_{ijk} \tag{9}$$

Material properties and load intensity as the essential and voxel-wise changing quantities are uniquely identified by the indices i, j, k that are used to define the integration limits for each voxel integral, according to the normalized coordinate directions ξ, η, ζ

$$t_{\xi,i} = -1.0 + 2\,\tfrac{i-1}{n_z} \qquad i = 1, \ldots, n_z \tag{10}$$

$$t_{\eta,j} = -1.0 + 2\,\tfrac{j-1}{n_y} \qquad j = 1, \ldots, n_y \tag{11}$$

$$t_{\zeta,k} = -1.0 + 2\,\tfrac{k-1}{n_x} \qquad k = 1, \ldots, n_x \tag{12}$$

The voxel integrals then follow as

$$\mathbf{K}_{ijk} = \int_{t_{\xi,i}}^{t_{\xi,i+1}} \int_{t_{\eta,i}}^{t_{\eta,i+1}} \int_{t_{\zeta,i}}^{t_{\zeta,i+1}} \mathbf{B}^T \alpha\, \mathbf{C}_{ijk}\, \mathbf{B}\; det\mathbf{J}\, d\zeta d\eta d\xi \tag{13}$$

$$\mathbf{P}_{ijk} = \int_{t_{\xi,i}}^{t_{\xi,i+1}} \int_{t_{\eta,i}}^{t_{\eta,i+1}} \int_{t_{\zeta,i}}^{t_{\zeta,i+1}} \mathbf{N}^T \alpha\, \mathbf{p}_{ijk}\; det\mathbf{J}\, d\zeta d\eta d\xi \tag{14}$$

In the special case of isotropic material properties, the elasticity matrix $\mathbf{C}_{ijk}$ for each voxel can be further split into two independent parts according to the Lamé constants λ_{ijk} and μ_{ijk} (see [4])

$$\mathbf{C}_{ijk} = \lambda_{ijk}\, \mathbf{C}^\lambda + \mu_{ijk}\, \mathbf{C}^\mu \tag{15}$$

where

$$\mathbf{C}^{\lambda} = \begin{bmatrix} 1 & 1 & 1 & 0 & 0 & 0 \\ 1 & 1 & 1 & 0 & 0 & 0 \\ 1 & 1 & 1 & 0 & 0 & 0 \\ 0 & 0 & 0 & 0 & 0 & 0 \\ 0 & 0 & 0 & 0 & 0 & 0 \\ 0 & 0 & 0 & 0 & 0 & 0 \end{bmatrix} \quad \text{and} \quad \mathbf{C}^{\mu} = \begin{bmatrix} 2 & 0 & 0 & 0 & 0 & 0 \\ 0 & 2 & 0 & 0 & 0 & 0 \\ 0 & 0 & 2 & 0 & 0 & 0 \\ 0 & 0 & 0 & 1 & 0 & 0 \\ 0 & 0 & 0 & 0 & 1 & 0 \\ 0 & 0 & 0 & 0 & 0 & 1 \end{bmatrix} \tag{16}$$

are constant matrices (Eq. (13)) and can therefore be written as

$$\hat{\mathbf{K}}_c \;=\; \sum_{i=1}^{n_z} \sum_{j=1}^{n_y} \sum_{k=1}^{n_x} (\lambda_{ijk}\, \mathbf{K}^{\lambda}_{ijk} + \mu_{ijk}\, \mathbf{K}^{\mu}_{ijk}). \tag{17}$$

It is worth to note that the new defined quantities $\mathbf{K}^{\lambda}_{ijk}$, $\mathbf{K}^{\mu}_{ijk}$ are independent of the voxel-wise material properties and can be pre-computed in dependence of the polynomial degree of the Ansatz, the number of voxels per cell ($n_x \times n_y \times n_z$) and the voxel spacing (s_x, s_y, s_z). Thus the impact of changing material properties during the simulation of structures reduces to a modification of the Lamé constants that simply scale the pre-computed voxel stiffness, followed by summation over all stiffness contributions. Contributions from the extension domain are penalized with α as defined in (1).

For qCT-derived voxel models the spacing of the voxels depends on the spatial resolution of the CT-scanner. Assuming the same voxel spacing $s_x = s_y$ in the $x-y$-plane of each qCT-slice the dependence of the quantities $\mathbf{K}^{\lambda}_{ijk}$ and $\mathbf{K}^{\mu}_{ijk}$ reduces from the three parameters s_x, s_y, s_z to two parameters r, s_z.

$$\mathbf{K}^{\lambda}_{ijk} \;=\; s_z\, (\mathbf{K}^{\lambda_0}_{ijk} + r\, \mathbf{K}^{\lambda_1}_{ijk} + r^2\, \mathbf{K}^{\lambda_2}_{ijk}) \tag{18}$$

$$\mathbf{K}^{\mu}_{ijk} \;=\; s_z\, (\mathbf{K}^{\mu_0}_{ijk} + r\, \mathbf{K}^{\mu_1}_{ijk} + r^2\, \mathbf{K}^{\mu_2}_{ijk}) \tag{19}$$

with $r := s_x/s_z$, thus valid for any type of qCT-scan [37].

The voxel integrals are solved numerically applying a $p+1$ point Gauss-integration. For many applications the pre-computation scheme for the fine ($n_x \times n_y \times n_z$) voxel resolution can be replaced by a coarser resolution of ($m_x \times m_y \times m_z$) sub-cells, each representing a chunk of $((n_x/m_x) \times (n_y/m_y) \times (n_z/m_z))$ voxels with averaged properties when indicated.

Figure 2 provides an overview about the storage requirements of the pre-computed matrices of the present implementation that exploits the hierarchic shape functions of the p-version trunk space [32, 30].

3.2 Efficiency analysis

The following academic example gives an impression about the efficiency of the pre-computation approach for time-critical computations such as e.g. user-interactive simulations [38]. The computational model consists of 1000 finite cells each covering $10 \times 10 \times 10$ voxel. The example

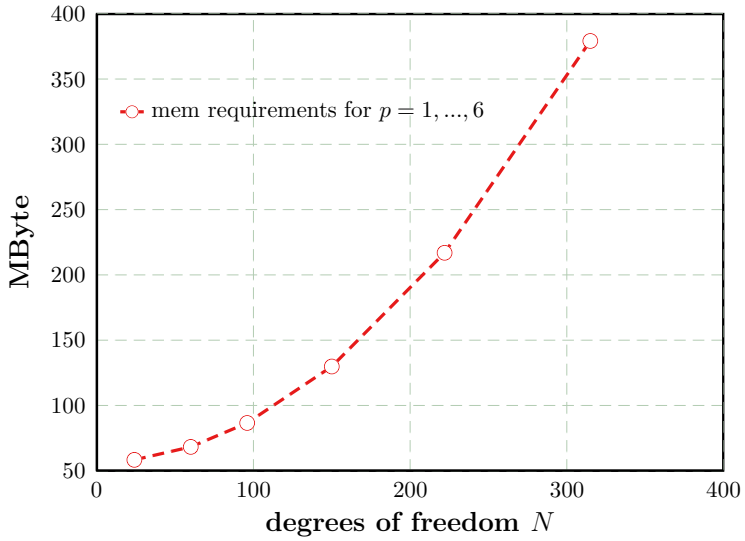

Figure 2: Memory allocation of the precomputed matrix $\mathbf{K}^{\lambda_0}$ for increasing polynomial degree with fixed resolution of $10 \times 10 \times 10$ voxel per finite cell. For the complete pre-computed stiffness matrix $\mathbf{K}_c$ the shown values increase by a factor 6.

compares the computation time of the pre-computation approach and a standard FCM integration scheme [10] based on 10^3 sub-cells each integrated with $(p+1)^3$ quadrature points.

Table 1 gives an overview about the computation times for the competing integration schemes, revealing an acceleration factor that scales weakly superlinear with the number of degrees of freedom. It has to be mentioned that for this comparison and for the comparisons of all following examples the measurements for the pre-computation scheme assume that the set of pre-computed matrices is already available. With the scheme derived in the previous sections the pre-computation of the voxel integral contributions is widely generalized for various voxel data. The time-consuming pre-computation only depends on the polynomial degree p and the number $(m_x \times m_y \times m_z)$ of sub-cells per finite cell used for integration. This effort corresponds to the results shown in column 3 of Table 1.

4 Numerical examples

The following examples were selected to verify the performance of the proposed method in terms of accuracy and numerical efficiency. All computations were performed with the p-FEM-analysis platform *AdhoC* [12] that has been extended by an implementation of the pre-computation concept. All examples focus on reduction of the numerical effort for the computation of the cell-stiffness. The granularity level for all computations is either set to $(5 \times 5 \times 5)$ or $(10 \times 10 \times 10)$ voxel per finite cell.

Computation time (s)			
p-deg.	**pre-computation**	**sub-cell integration**	**accel. factor**
1	0.14	38	271
2	0.82	362	441
3	2.04	1521	746
4	5.09	5755	1130
5	11.19	18430	1647
6	22.46	49577	2207

Table 1: Computation time for the pre-computation scheme and a standard FCM Gauss quadrature on 10^3 sub-cells/finite cell.

4.1 Unit cube with heterogeneous material properties

The pre-computation concept of section 3.1 allows the use of various integration methods to solve the governing integral equations. In [37] the symbolic computation framework *GiNaC*[5] was used to exactly pre-compute the cell stiffness. In this contribution we basically focus on numerical integration by Gauss quadrature. It is worth to mention that due to the orthogonal cell structure of the Finite Cell Method, the polynomial character of the Ansatz functions is preserved in the governing integral equations, thus allowing exact integration with $(p+1)$ quadrature points for each coordinate direction. With the following benchmark problem, developed in [24], the

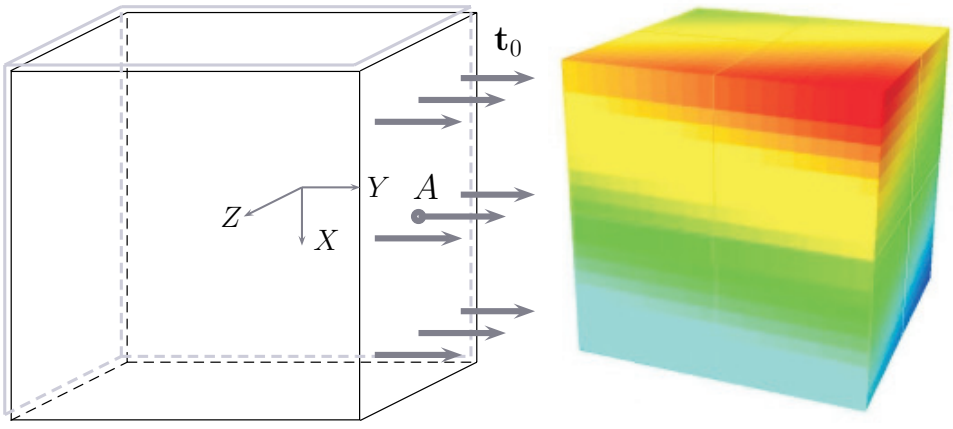

Figure 3: Geometry and symmetry boundary conditions at faces $x = -0.5$, $y = -0.5$ and $z = 0$ of a unit cube model (left), discrete heterogeneous distribution of the Young's modulus (right). Location A marks the point of interest that was considered in the analysis.

accuracy of the method is demonstrated and it is further shown that due to the decomposition of the governing integrals into sub-integrals, reduced integration schemes are applicable without

loss of accuracy thus reducing the numerical effort significantly. A two-point Gauss quadrature and the Simpson rule are applied exemplarily to demonstrate the well-behaving performance for low order integration.

We consider a voxelized unit cube of heterogeneous material properties that was derived from a continuous model, generated with the relation $E = (x + 10)^2(y + 10)(z + 1)\ [N/mm^2]$ for the Young's modulus and a constant Poisson ratio of $\nu = 0.3$. Geometry and boundary conditions are provided in Figure 3.

For the FCM approach the cube is discretized into $2 \times 2 \times 2$ cells where each cell contains $10 \times 10 \times 10$ voxel. For each voxel a Young's modulus is computed from the above equation and the corresponding value is assumed to be constant within the voxel. Based on this FCM discretization a p-extension with $p = 1, 2, 3, \ldots, 8$ is performed applying the pre-computation scheme.

Diagram 4a reveals the modeling error of the applied voxel resolution with respect to the continuous model following the given material distribution function for E. The diagram shows the relative error in energy norm e_r for a uniform p-refinement of the voxelized cube model and the continuous model

$$e_r = \sqrt{\frac{|\mathcal{U}_{EX} - \mathcal{U}_{FCM}|}{\mathcal{U}_{EX}}} \times 100\ \ [\%] \tag{20}$$

with $\mathcal{U}_{EX/FCM}$ denoting the strain energy of the exact solution and the numerical approximation, respectively. The reference value $\mathcal{U}_{EX}$ for both curves was extrapolated from the p-FEM solution for the polynomial degrees $p = 8, 9, 10$.

Diagram 4b shows the accuracy of the pre-computation scheme for various integration schemes with regard to the exactly integrated solution with the composed sub-cell integration scheme shown in [24, 10]. The result of the pre-computation scheme exactly meets the solution of the composed sub-cell integration, as it was expected from section 3.1. The numerical effort for the pre-integration of the cell stiffness was significantly reduced by a decrease of the number of quadrature points for the sub-integrals of (13). Two quadrature points in each local direction of the sub-cell proved to be sufficient for all applied polynomial degrees to achieve solutions without any noticeable error in energy norm. An analogous result was observed for the application of the Simpson rule. For both methods identical results were achieved for all polynomial degrees (Fig. 4b).

Figure 5 illustrates the convergence of the cube example in terms of the displacements u_x, u_z (Diagram 5b (left)) and u_y (Diagram 5b (right)) for reference point A and the relative error of the displacements u_y (Diagram 5a) for a uniform p-refinement. The diagrams show curves for all tested integration schemes with almost identical results. The only slight deviation of $< 0.4‰$ of the Simpson rule from the Gauss quadrature results is noticeable in diagram 5a for the polynomial degrees 7 and 8.

4.2 Trabecular bone biopsy model

In the following example a specimen of human trabecular bone is analyzed. The example was chosen to demonstrate the accuracy and efficiency of the pre-computation approach for a highly

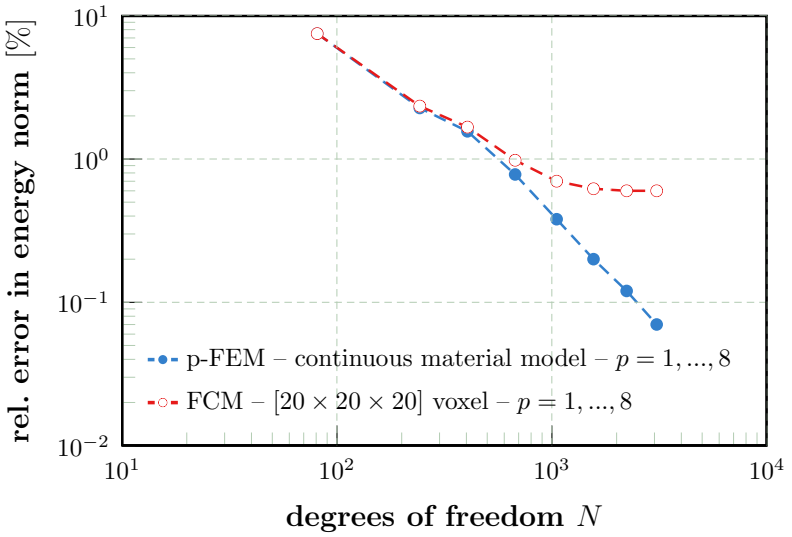

(a) Modeling error of the voxelized cube model.

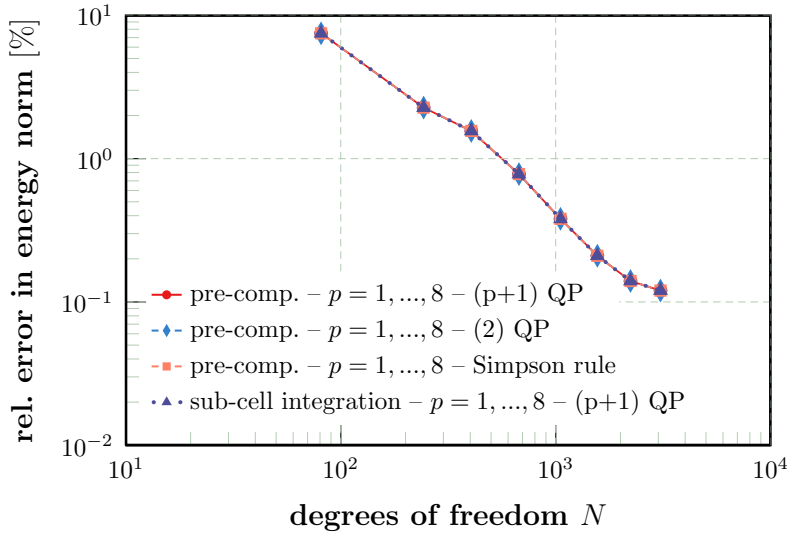

(b) Convergence study of the pre-computation method for various reduced numerical integration schemes compared with the solution for full Gauss integration applying $(p+1)^3$ quadrature points (QP).

Figure 4: Error and convergence analysis of the voxel-cube benchmark.

complex geometry in comparison to the analysis with the classical h-FEM. A reference solution has been computed with the FCM and compared to a standard h-version FEM in [10]. The material properties and boundary conditions are provided in Figure 6.

For a comparison the reaction force of the upper surface of the bone model is computed. The

original model shown in Figure 6 is provided as a triangulated surface given in STL format* from BARUFFALDI AND PERILLI [3]. The Finite Element reference solution was obtained from an analysis with the commercial software ABAQUS [29] applying 10-node tetrahedral elements†. Several tetrahedral meshes of various densities were generated with the mesh generator NETGEN [27]. Table 2 provides the time effort for mesh generation and analysis of all generated FE-models. The reference FE-solution converges to a vertical reaction force of approximately

		Time effort (s)		
refinem.	**# Elements**	Mesh gen.	Analysis	Total
1	23450	405	23	428
2	37050	388	43	431
3	81206	482	151	633
4	300611	2300	1006	3306
5	480679	7516	2160	9676
6	1577863	8159	14410	22569
7	3437623	12083	43431	55514

Table 2: Time effort for mesh generation (NETGEN) and h-FEM analysis (ABAQUS) of the human biopsy model, measured on a single core AMD Opteron 250 (2.4GHz)

$-2470N$.

For the analysis with the Finite Cell Method four voxel models of various resolutions were generated with an octree-based voxel decomposition [36]. The various resolutions and corresponding results obtained from the pre-computation scheme analysis are provided in Figure 7.

The convergence curves of the reaction forces are obtained with a uniform p-refinement. The coarser models (A and B) applied $5 \times 5 \times 5$ voxels per finite cell while the finer models (C and D) were analyzed with $10 \times 10 \times 10$ voxels per finite cell. With convergence to a value of $-2430N$ the reaction force of the models C and D stay below a relative error of 2%.

The implementation of the FCM with pre-computation scheme was parallelized for multi-core architectures applying the OpenMP library [7] to exploit full performance of the developed method. Figure 8 shows the parallel efficiency for the computation of the stiffness of model C for polynomial degrees up to order 6. The efficiency clearly increases with the size of the cell matrices and settles down at $\sim 80\%$ and reaches a maximum of 87% at $p = 3$. The code parallelization includes also the assembly and the solution of the governing system of equations (not part of Fig. 8). Whereas the assembly effort remains nearly constant, the solver profits from the parallel approach by a factor of ~ 3.

*The STL format is frequently applied in rapid prototyping and it is used to interact with stereo-lithography machines

†ABAQUS element type: C3D10, quadratic tetrahedron, full integration

The total computational time effort of the converged solution of $2430N$ at $p = 6$ (Fig. 7, curve C) was measured on a 8 core -Intel Xeon W5590, 3.33GHz work station with $145s$. A comparable model size ($\sim$ 300000 degrees of freedom) from the NETGEN/ABAQUS analysis showed a total computational time effort of $\sim 3300s$ (single core AMD Opteron 250, 2.4GHz) including mesh generation and analysis. The analysis result of $2482N$ for this model had not yet converged to the reference value of $2470N$ and required another four refinement steps until convergence to the final solution was observable with a total time effort of more than 15 hours.

4.3 Validated femur analysis

The following example simulates the elastic behavior of a human proximal femur under compression. With this example we demonstrate the potential of the method to accurately predict the in-vivo bone strength of a human femur. The numerical results are validated by an in-vitro experiment by YOSIBASH et al. [41]. In particular the example shows that the simulation of the qCT-scanned fresh frozen femur bone can be performed without a time-consuming segmentation.

Figure 9(a) shows the setup of the experiment. The femur is loaded with a $1000N$ compression load on the femur head and fully clamped at its distal face. Four uniaxial strain gauges are installed on the bone surface to measure surface strains at the femoral neck (SG1), the greater trochanter (SG2) and the lateral shaft (SG3, SG4). The vertical displacement is measured with a LVDT[‡] installed at the plunger of the testing machine.
The numerical model was derived from a qCT-scan (Fig.9(b)) with a resolution of $512\times512\times200$ voxel and a spacing of $0.78125mm$ in the $x-y$-plane of the qCT-slices and $0.75mm$ in z-direction. The bone is embedded in 667 finite cells, each covering $10 \times 10 \times 10$ voxel (Fig.9(c)). The boundary conditions are applied according to the experiment. Heterogeneous isotropic material properties are derived from a linear conversion of the Hounsfield Unit distribution obtained from the qCT-scan in an equivalent mineral density, calibrated by a scanned phantom device.

$$\rho_{EQM} = 10^{-3}\,(0.6822\,HU - 5.48) \quad [g/cm^3] \tag{21}$$

With (21) the Young's modulus for each voxel of the cortical and trabecular bone regions were found according to the relation [15]

$$E = 10200\,(1.22\,\rho_{EQM} + 0.0523)^{2.01} \qquad \text{if } HU \leq 500 \tag{22}$$

$$E = 5307\,(1.22\,\rho_{EQM} + 0.0523) + 469 \qquad \text{if } HU > 500 \quad [MPa] \tag{23}$$

Previous studies confirm that isotropic material properties suffice to obtain accurate results for this type of simulation [2, 22, 24].
The FCM analysis was performed for a polynomial degree of $p = 4$. At this p-degree the analysis showed a relative error in energy norm of 8% (Figure 10). A reference value for the relative error estimate was found from extrapolation of the strain energy values at $p = 4, 5, 6$.
Figure 11 shows the von Mises stress distribution from a computation with $p = 4$ along a vertical and horizontal cut through the femur that reveals stress concentrations in the lower femoral neck and the medial shaft area.

		Uz	SG1	SG2	SG3	SG4
Experiment		-300	-1303	440	-1303	441
Finite Cell Method	point-wise	-295	-1249	806	-1171	436
	error[%]	1.67	4.14	83.18	10.13	0.91
	surface-avg.	NA	-1246	765	-1154	440
	error[%]	NA	4.37	73.86	11.43	0.22

Table 3: Comparison of predicted and measured results and relative errors with respect to the experiment for a polynomial degree $p = 4$.

Table 3 compares the numerical prediction and the in-vitro experiment for surface strains $[\mu\epsilon]$ and the vertical displacement $[\mu m]$. The comparison includes pointwise values in terms of principal strains and surface averaged results obtained from several point results in the close vicinity of the strain gauge location. The results show good agreement between the predicted and measured values of the experiment. Location 2 is identified as outlier result most probably due to insufficient reading of the strain gauge. Numerical results that were found by a p-FEM analysis in [40] confirm the result as outlier and indicate a high sensitivity of the near neighborhood for this location. Even with the outlier included a linear regression analysis provides a very good correlation of the results with a correlation factor $R^2 > 0.92$.
Measured on an Intel Xeon W5590, 3.33GHz work station with 8 cores, the total computational time for the femur model (computed with $p = 4$) was below 10 seconds. In [38] it is shown that for a slightly coarser cell model ($p = 4$) an accurate and reliable solution can be retrieved with update rates below one second thus satisfying the requirements for responsive user interactive simulations.

5 Summary and conclusions

This paper has introduced a pre-computation scheme for voxel-based data models as an extension to the Finite Cell Method. The method is particularly able to handle geometric highly complex structures and problems with multi-material interfaces such as biological hard-tissue at negligible effort for modeling and simulation. Due to a fictitious domain approach of the Finite Cell Method the structure is embedded in a geometric simple domain of computation that is created on a Cartesian grid with no need for explicit, time-consuming and often error-prone mesh generation. Instead, the method exploits the structural and topological properties of the Cartesian grid and the voxel data. It is shown that the effort for the numerical evaluation of the governing cell

[‡]linear variable displacement transducer

integrals can be significantly reduced by a generalized, pre-computed set of matrices and vectors independent of any physical properties, only depending on geometric aspects. With the pre-computed data the true physical properties as stiffness and volume load are approximated at high accuracy and reduced cost in terms of time complexity. A specialization of the pre-computation scheme to qCT-derived voxel data enables a formulation that is independent of machine-specific characteristics of the scanner and provides a powerful tool for the analysis and simulation of structures with heterogeneous material properties as this is the case for any soft and hard tissue from biomedical applications. This approach has particularly proven to produce sufficient update rates for user-interactive simulations in a computational steering environment for patient specific surgery preparation [38], even for higher polynomial degrees. The implementation of the pre-computation scheme is parallelized for multi-core architectures and shows a parallel efficiency close to 90% on eight cores.
Accuracy, reliability and numerical efficiency is demonstrated with several examples. Due to the applied hierarchical high-order Ansatz spaces of the Finite Cell Method a uniform refinement of the polynomial degree can be easily performed during runtime to reduce the numerical error and to obtain numerically reliable results. Validation data from a femur experiment have proven to well correlate with the numerical prediction of the elastic response of the loaded femur in terms of strains and displacements thus underlining the high quality of the converged simulation results. A comparison of a FCM analysis with the modeling and simulation procedure of a standard h-FEM software reveals a dramatic improvement in terms of model generation and analysis. The Finite Cell approach shows a high potential for time-critical problems of voxel-based data models to significantly increase the performance of the simulation pipeline.

Acknowledgment
This work has been supported by the SIEMENS AG and TUM International Graduate School of Science and Engineering (IGSSE). This support is gratefully acknowledged. The authors would like to thank Prof. Z. Yosibash and his group from the Ben-Gurion University of the Negev, Israel, for providing the experimental femur results for validation and for the great help and support while performing the numerical tests.

References

[1] T. Adachi, K. Hiromichi, and T. Yoshihiro. Shape optimization based on traction method using voxel-fem. *Transactions of the Japan Society of Mech. Engineers*, 70(691):426–433, 2004.

[2] V. Baca, Z. Horak, P. Mikulenka, and V. Dzupa. Comparison of an inhomogeneous orthotropic and isotropic material models used for fe analyses. *Med. Eng. Phys*, 30:924–930, 2008.

[3] F. Baruffaldi and E. Perilli. Human bone biopsy, 3D model Bn_326_3D.stl, From: The BEL Repository. http://www.tecno.ior.it/VRLAB/.

[4] K.-J. Bathe. *Finite Element Procedures*. Prentice Hall, Inc, 1996.

[5] C. Bauer, A. Frink, V. V. Kisil, K. Richard, and A. Sheplyakov. GiNaC is Not a CAS. http://www.ginac.de/.

[6] Q. Cai, S. Kollmannsberger, R.P. Mundani, and E. Rank. The finite cell method for solute transport problems in porous media. In *Proc. of the 16th Int. Conference on Finite Elements in Flow Problems*, 2011.

[7] B. Chapman, G. Jost, and R. van der Pas. *Using OpenMP. Portable Shared Memory Parallel Programming*. MIT Press, 2008.

[8] C. Dick, J. Georgii, R. Burgkart, and R. Westermann. Stress Tensor Field Visualization for Implant Planning in Orthopedics. *IEEE Transactions on Visualization and Computer Graphics*, 15(6):1399–1406, 2009.

[9] A. Düster, J. Parvizian, and E. Rank. Topology optimization based on the finite cell method. *Proceedings in Applied Mathematics and Mechanics*, 10:151–152, 2010.

[10] A. Düster, J. Parvizian, Z. Yang, and E. Rank. The finite cell method for three-dimensional problems of solid mechanics. *Computer Methods in Applied Mechanics and Engineering*, 197:3768–3782, 2008.

[11] A. Düster, H.-G. Sehlhorst, and E. Rank. Numerical homogenization of heterogeneous and cellular materials utilizing the finite cell method. *Computational Mechanics*, submitted, 2011.

[12] A. Düster and M. Rücker. *AdhoC^3 – User's Guide*. Lehrstuhl für Bauinformatik, Technische Universität München, 2001.

[13] J. Frisch and R.P. Mundani. Multiskalen-Strömungssimulation eines Kraftwerkskomplexes auf Höchstleistungsrechnern. In *Proc. 22. Forum Bauinformatik, Berlin 2010*, 2010.

[14] T. Gunter, B. Merz, R. Merieske-Stern, J. Schmitt, R. Leppek, and M. Lengesfeld. Zahnimplantattestung am in-vivo-finite-elemente-modell - testing of dental implants using an in vivo finite element model. *Biomedizinische Technik/Biomedical Engineering*, 45(10):272–276, 2000.

[15] J. H. Keyak and Y. Falkinstein. Comparison of in situ and in vitro CT scan-based finite element model predictions of proximal femoral fracture load. *Medical Engineering and Physics*, 25(9):781–787, 2003.

[16] K. Koketsu, H. Fujiwara, and Y. Ikegami. Finite-element simulation of seismic ground motion with a voxel mesh. *Pure and Applied Geophysics*, 161:2183–2198, 2004.

[17] M. Lengsfeld, J. Schmitt, P. Alter, J. Kaminsky, and R. Leppek. Comparison of geometry-based and ct voxel-based finite element modelling and experimental validation. *Med. Eng. Phys.*, 20(7):515–522, 1998.

[18] P. Magne. Efficient 3d finite element analysis of dental restorative procedures using micro-ct data. *Dental Materials*, 23(5):539–548, 2007.

[19] S. Margenox and Y. Vutov. Comparative analysis of pcg solvers for voxel fem systems. In *Proc Int'l Multiconference Comp. Science Information Techn.*, pages 591–598. 2007.

[20] J. Parvizian, A. Düster, and E. Rank. Finite cell method – h- and p-extension for embedded domain problems in solid mechanics. *Comput. Mech.*, 41:121–133, 2007.

[21] J. Parvizian, A. Düster, and E. Rank. Topology optimization using the finite cell method. *Optimization and Engineering*, DOI 10.1007/s11081-011-9159-x, 2011.

[22] L. Peng, J. Bai, Z. Zeng, and Y. Zhou. Comparison of isotropic and orthotropic material property assignments on femoral finite element models under two loading conditions. *Med. Eng. Phys.*, 28:227–233, 2006.

[23] E. Perilli, F. Baruffaldi, M. Visentin, B. Bordini, F. Traina, A. Cappello, and M. Viceconti. MicroCT examination of human bone specimens: effects of polymethylmethacrylate embedding on structural parameters. *Journal of Microscopy*, 225:192–200, 2007.

[24] M. Ruess, D. Tal, N. Trabelsi, Z. Yosibash, and E. Rank. The finite cell method for bone simulation: Verification and validation. *Biomechanics and Mechanobiology*, DOI 10.1007/s10237-011-0322-2, 2011.

[25] D. Schillinger, A. Düster, and E. Rank. The hp-d adaptive finite cell method for geometrically nonlinear problems of solid mechanics. *International Journal for Numerical Methods in Engineering*, DOI 10.1002/nme.3289, 2011.

[26] D. Schillinger and E. Rank. An unfitted hp-adaptive finite element method based on hierarchical b-splines for interface problems of complex geometry. *submitted to Computer Methods in Applied Mechanics and Engineering*, 2011.

[27] J. Schöberl. NETGEN. http://www.hpfem.jku.at/netgen/index.html.

[28] H.-G. Sehlhorst, A. Düster, R. Jänicke, S. Diebels, and E. Rank. Extraction of effective material parameters with application to sandwich structures. *Proceedings in Applied Mathematics and Mechanics*, submitted,2011.

[29] SIMULIA. ABAQUS. http://www.simulia.com/products/abaqus_standard.html.

[30] B. Szabó and I. Babuška. *Finite Element Analysis*. John Wiley & Sons, New York, 1991.

[31] B. A. Szabó and I. Babuška. *Finite Element Analysis*. John Wiley & Sons, 1991.

[32] B. A. Szabó, A. Düster, and E. Rank. The p-version of the Finite Element Method. In E. Stein, R. de Borst, and T. J. R. Hughes, editors, *Encyclopedia of Computational Mechanics*, volume 1, chapter 5, pages 119–139. John Wiley & Sons, 2004.

[33] T. Torigaki and K. Fujitani. Power of a voxel approach to structural analysis and topology-shape optimization in automobile industries. *Japan J. Indust. App. Math.*, 17:129–147, 2000.

[34] B. van Rietbergen, H. Weinans, and R. Huiskes. Computational Strategies for Iterative Solutions of Large FEM Applications Employing Voxel Data. *International Journal for Numerical Methods in Engineering*, 39:2743–2764, 1996.

[35] C. Vinci. *Application of Dirichlet Boundary Conditions in the Finite Cell Method*. Master thesis, Lehrstuhl für Computation in Engineering, Fakultät für Bauingenieur- und Vermessungswesen, Technische Universität München, 2009.

[36] P. Wenisch, C. van Treeck, A. Borrmann, E. Rank, and O. Wenisch. Computational steering on distributed systems: indoor comfort simulations as a case study of interactive cfd on supercomputers. *Int'l Journal of Parallel, Emergent and Distributed Systems*, 22:275–291, 2007.

[37] Z. Yang. *The Finite Cell Method for Geometry-Based Structural Simulation*. PhD thesis, Lehrstuhl für Computation in Engineering, Fakultät für Bauingenieur- und Vermessungswesen, Technische Universität München, 2011.

[38] Z. Yang, S. Kollmannsberger, A. Düster, M. Ruess, E. Grande Garcia, R. Burgkart, and E. Rank. Non-standard bone simulation: Interactive numerical analysis by computational steering. *Computing and Visualization*, submitted for publication, 2011.

[39] Z. Yosibash, R. Padan, L. Joscowicz, and C. Milgrom. A CT-based high-order finite element analysis of the human proximal femur compared to in-vitro experiments. *ASME Journal of Biomechanical Engineering*, 129:297–309, 2007.

[40] Z. Yosibash, N. Trabelsi, and C. Milgrom. Reliable simulations of the human proximal femur by high-order finite element analysis validated by experimental observations. *Journal of Biomechanics*, 40:3688–3699, 2007.

[41] Z. Yosibash, N. Trabelsi, and C. Milgrom. Reliable simulations of the human proximal femur by high-order finite element analysis validated by experimental observations. *Journal of Biomechanics*, 40:3688–3699, 2007.

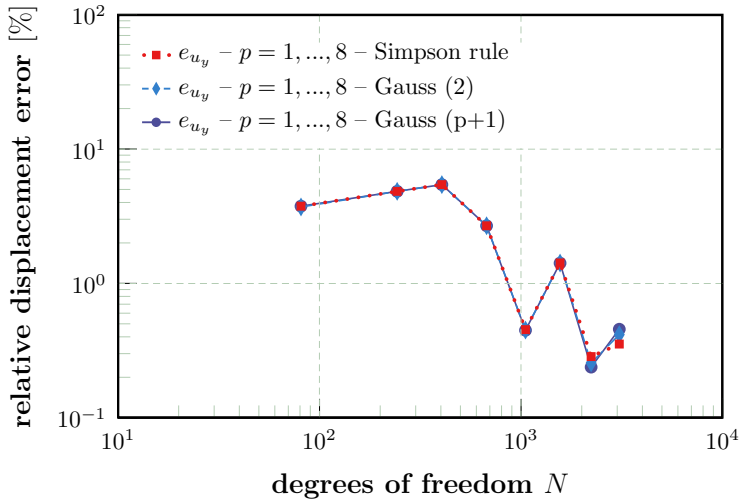

(a) Relative error of u_y

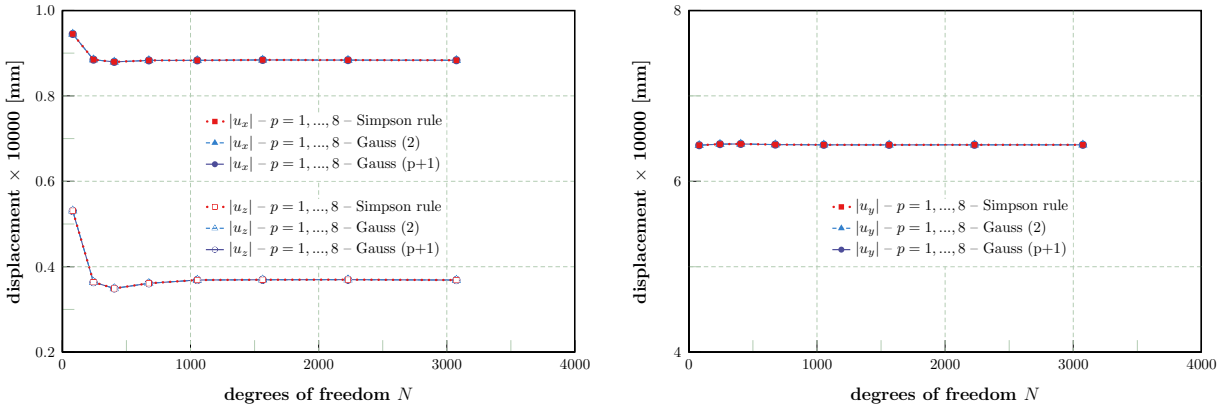

(b) Convergence of the displacements u_x, u_y and u_z

Figure 5: Performance study at point A for various integration schemes.

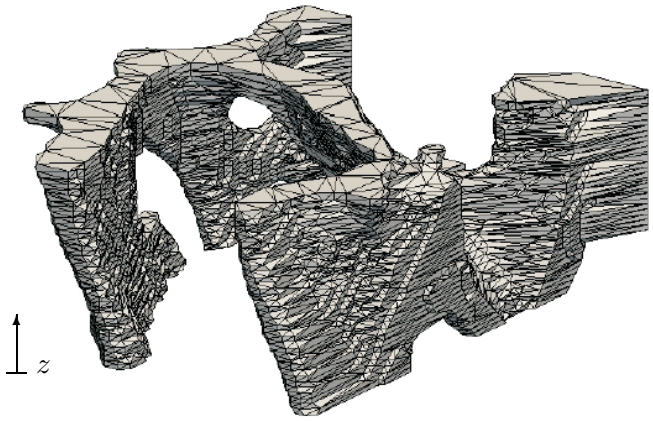

Figure 6: Substructure of a human trabecular biopsy model with homogeneous isotropic material properties. The bone fragment is loaded on top with a prescribed displacement $\mathbf{u}_0$ and fully clamped on the bottom face ($z = 0$). The analysis provides the reaction force of the upper surface for comparison.

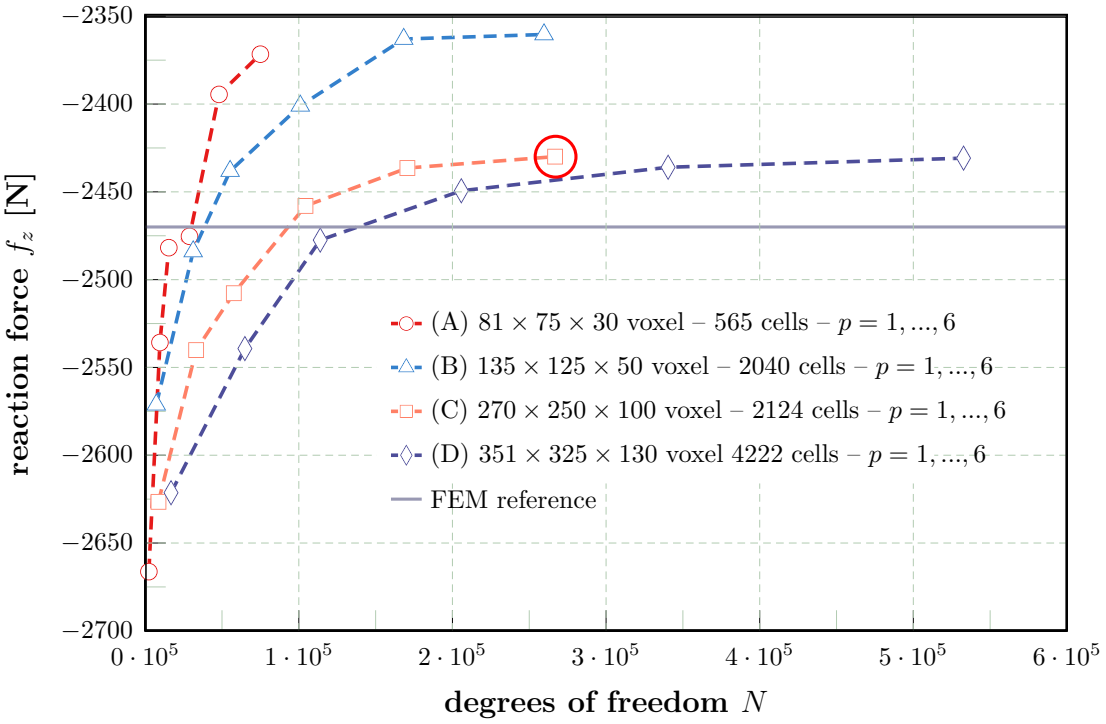

Figure 7: Convergence plots for the FCM pre-computation analysis scheme of the human bone biopsy model indicating the total number of voxel and corresponding number of embedding finite cells.

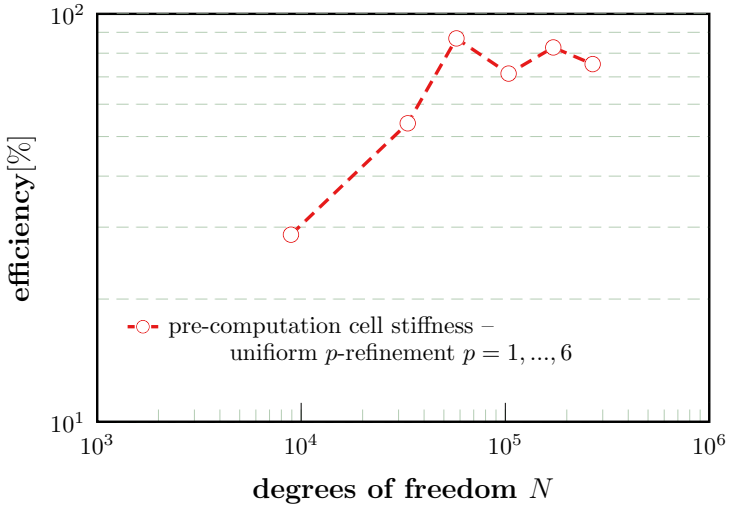

Figure 8: Parallel efficiency of the multi-core parallel pre-computation of the model stiffness on 8 cores for a uniform p-refinement.

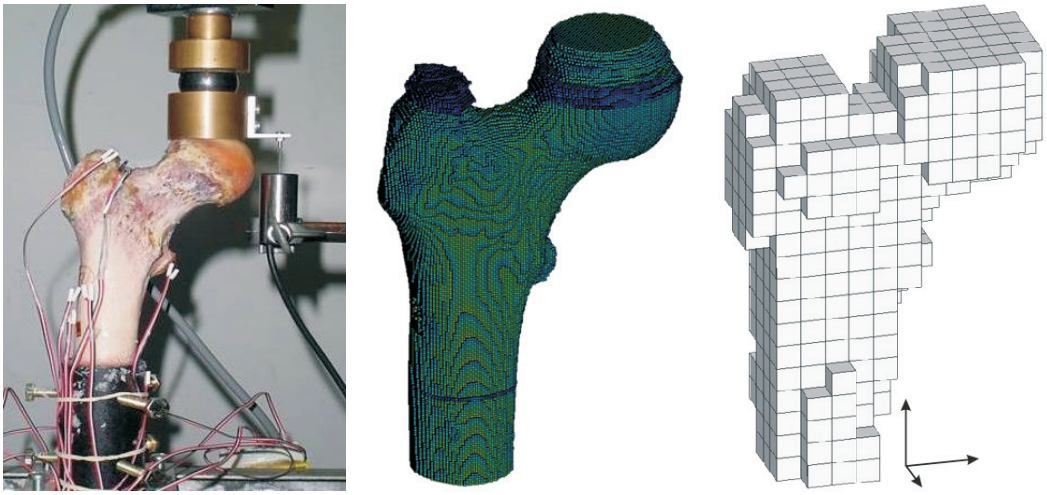

(a) (b) (c)

Figure 9: In-vitro experiment setup (a), qCT-voxel model of the proximal femur (b), finite cell model (c)

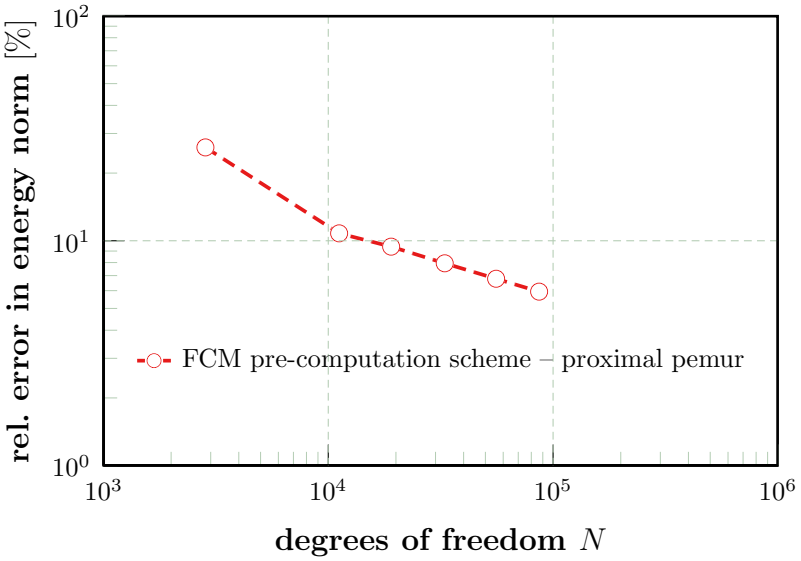

Figure 10: Convergence of the FCM analysis of the proximal femur: Relative error in energy norm for a uniform p-refinement $(p = 1, ..., 6)$

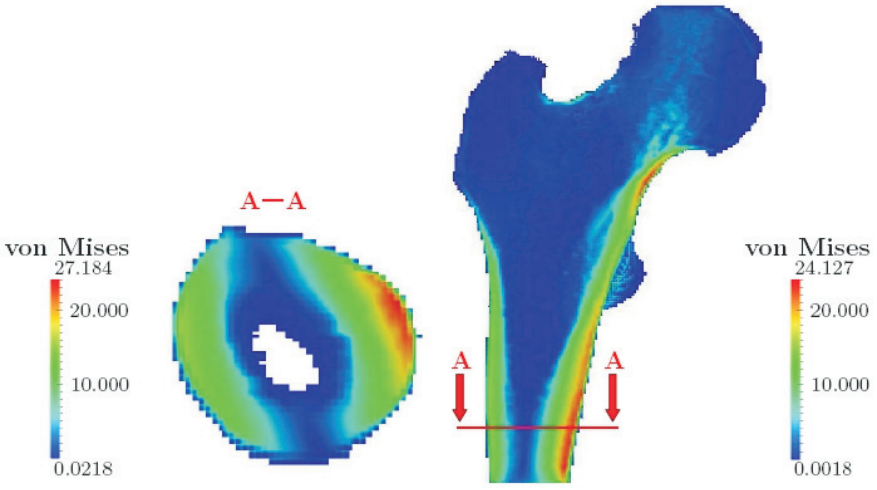

Figure 11: Voxelplot of the von Mises stress distribution of the proximal femur loaded on top with $1000N$